



Abundance Measurements of the Metal-poor M Subdwarf LHS 174 Using High-resolution Optical Spectroscopy

Neda Hejazi^{1,2} , Sébastien Lépine² , Thomas Nordlander³ , Wei-Chun Jao² , David R. Coria¹ , and Kathryn V. Lester⁴

¹Department of Physics and Astronomy, University of Kansas, Lawrence, KS 66045, USA; nhejazi@ku.edu

²Department of Physics and Astronomy, Georgia State University, Atlanta, GA 30303, USA

³Theoretical Astrophysics, Department of Physics and Astronomy, Uppsala University, Box 516, 751 20 Uppsala, Sweden

⁴Department of Astronomy, Mount Holyoke College, South Hadley, MA 01075, USA

Received 2025 March 21; revised 2025 April 27; accepted 2025 April 28; published 2025 June 6

Abstract

Metal-poor M subdwarfs are among the oldest stellar populations and carry valuable information about the chemical enrichment history of the Milky Way. The measurements of chemical abundances of these stars therefore provide essential insights into the nucleosynthesis in the early stages of the Galaxy's formation. We present detailed spectroscopic analysis of a nearby metal-poor M subdwarf, LHS 174, from its high-resolution optical spectrum, and apply our previously developed spectral fitting code, `AutoSpecFit`, to measure the abundances of five elements: $[O/H] = -0.519 \pm 0.081$, $[Ca/H] = -0.753 \pm 0.177$, $[Ti/H] = -0.711 \pm 0.144$, $[V/H] = -1.026 \pm 0.077$, and $[Fe/H] = -1.170 \pm 0.135$. We compare the abundances of O, Ti, and Fe derived from this work and those from previous studies, and demonstrate the observed data are clearly better matched with the synthetic model generated based on our abundances than those from the other analyses. The accuracy of inferred stellar abundances strongly depends on the accuracy of physical parameters, which motivates us to develop a reliable technique to more accurately determine the parameters of low-mass M dwarfs and infer abundances with smaller uncertainties.

Unified Astronomy Thesaurus concepts: M dwarf stars (982); M subdwarf stars (986); Stellar abundances (1577)

1. Introduction

The stellar populations of the Milky Way are predominantly composed of low-mass M dwarfs, which constitute about $\sim 75\%$ of the total star count (see T. J. Henry & W.-C. Jao 2024 and references therein). M dwarfs have main-sequence lifetimes much longer than the age of the Universe, which means that their surface abundances have not been affected by the mixing (dredge-up) processes that alter the surface composition of evolved giant stars. In addition, atomic diffusion (G. Michaud et al. 1984) has a negligible effect on the atmospheric composition of M dwarfs (with deeper convection zones) as compared to more massive F, G, and K dwarfs (with shallower convection zones; X. S. Gao et al. 2018; M. Deal et al. 2020; N. Moedas et al. 2022; T. Nordlander et al. 2024). The chemical abundances of M dwarfs thus reflect the chemical composition of their progenitor molecular clouds, which makes them ideal tracers of the Galaxy's chemical enrichment history.

Although individual M dwarfs maintain a steady chemistry over time, given their long lifespans they have likely experienced gradual, long-term orbital migration within the Galaxy. Stellar orbits are, in general, subject to perturbations due to gravitational interaction with other stars or surrounding gas and dust as well as Galactic phenomena caused by spiral arms, giant molecular clouds, or other large-scale structures such as the tidal interaction of the Milky Way with a satellite galaxy. The orbital migration of stars may change the stellar distributions in various regions and affect the overall chemical structure of the Galaxy. In particular, the radial migration of stars in the disk can play an important role in the metallicity–age gradient across different radii (e.g., M. Haywood 2008;

R. Schönrich & J. Binney 2009). The study of long-lived M dwarfs in different stellar populations can therefore elucidate their migration history and provide crucial clues on Galactic chemodynamical evolution.

M dwarfs are primary targets for transit and radial velocity surveys of exoplanets, and are likely to host at least one orbiting planet (C. D. Dressing & D. Charbonneau 2013, 2015). Given their ubiquity and stable chemical pattern over time, M dwarfs can provide excellent sites to study star–planet chemical connections and probe the formation of planetary systems. However, only a handful of small M dwarf samples have reported abundances using careful high-resolution spectroscopy through spectral synthesis (D. Souto et al. 2017, 2022; C. Abia et al. 2020; Y. Shan et al. 2021; N. Hejazi et al. 2024; H. M. Tabernero et al. 2024). Most studies relevant to the chemical properties of stellar populations and star–planet compositional links have utilized the abundances of hotter F, G, and K dwarfs. The extension of such studies to numerous M dwarfs would reveal whether previously inferred trends have any dependence on stellar mass and if these trends are also valid in the low-mass regime. It is then of critical importance to develop reliable techniques to measure the abundances of M dwarfs.

The abundance analysis of M dwarfs has proven to be challenging. Owing to their intrinsic faintness, the acquisition of high signal-to-noise ratio (SNR), high-resolution spectra requires the use of large telescopes and long exposure times, which poses a costly observing time investment. Archival high-resolution M dwarf spectra are therefore limited to small samples of bright, nearby stars. Even with access to high-resolution, high-SNR M dwarf spectra, there are other challenges involved in constraining the chemical abundance of M dwarfs. For example, the spectra of M dwarfs are dominated by millions of molecular lines, mostly governed by TiO bands in the optical and H₂O bands in the near-infrared (NIR), which are blended with many crucial atomic lines.



Original content from this work may be used under the terms of the [Creative Commons Attribution 4.0 licence](https://creativecommons.org/licenses/by/4.0/). Any further distribution of this work must maintain attribution to the author(s) and the title of the work, journal citation and DOI.

In addition, this highly dense forest of molecular bands substantially obscures the smooth appearance of the true spectral continuum, making its identification difficult. Instead, we must work with a pseudo-continuum whose dependence on physical stellar parameters and chemical abundances is not the same as that of the true continuum. This demands a more meticulous treatment for spectroscopic analyses of M dwarfs compared to F, G, and K dwarfs that present a well-defined continuum in their spectra.

Low-metallicity M dwarfs, which are kinematically and chemically associated with the Galactic halo, are much less abundant than more metal-rich counterparts (making up $\sim 0.25\%$ of the total Galactic stellar population; I. N. Reid & S. L. Hawley 2000), and are, on average, farther away from the Sun and dimmer than disk stars. Consequently, only several small samples of metal-poor M dwarfs have been analyzed using high-resolution spectroscopy (V. M. Woolf & G. Wallerstein 2005, 2006; S. J. Schmidt et al. 2009; V. M. Woolf et al. 2009; A. S. Rajpurohit et al. 2014; V. M. Woolf & G. Wallerstein 2020), leaving the detailed properties of these stars largely unconstrained. On the other hand, larger samples have been studied using low-resolution spectroscopy, where metal-poor M dwarfs can be classified through a metallicity class sequence as (moderately metal-poor) M subdwarfs (sdM), extreme M subdwarfs (esdM), and ultra M subdwarfs (usdM) based on the relative strength of CaH bands with respect to the strength of TiO bands (see J. E. Gizis 1997; S. Lépine et al. 2007; N. Hejazi et al. 2020, 2022 and references therein).

In this study, we perform an in-depth, high-resolution analysis of a nearby (located at ~ 27 pc from the Sun) and relatively bright ($G = 12.035$), metal-poor M-type dwarf, LHS 174. The fundamental parameters, i.e., effective temperature (T_{eff}), surface gravity ($\log(g)$), overall metallicity ($[M/H]$), and microturbulence (ξ), have previously been determined for this star using high-resolution ($R \sim 33,000$) optical spectroscopy (V. M. Woolf & G. Wallerstein 2005, hereafter WW05). The synthetic model (generated using the method outlined in Section 4) based on the parameter values inferred from WW05 is in good agreement with the star's observed spectrum over many spectral regions (Sections 3 and 6). WW05 also measured the titanium and iron abundances of LHS 174 along with the above physical parameters via an iterative procedure. S. J. Schmidt et al. (2009, hereafter Sch09) then measured the oxygen abundance of the star using the physical parameters and the abundances of Ti and Fe from WW05 by employing molecular TiO lines (Sections 6 and 7). It should be noted that A. Y. Kesseli et al. (2019) have also reported the effective temperature and metallicity values for LHS 174 using its medium-resolution optical spectrum. While the effective temperature from A. Y. Kesseli et al. (2019) is in agreement with that of WW05, there is a significant difference in metallicity between these two studies (Table 1). We measure the abundances of the three elements O, Ti, and Fe using our newly developed pipeline, AutoSpecFit (N. Hejazi et al. 2024), and compare them with those from the previously used methodologies. We also infer the abundances of two additional elements, Ca and V, for this star using our method. In this pilot study, we apply AutoSpecFit, which was originally developed using high-resolution NIR spectra, to the high-resolution optical spectrum of LHS 174, showing the pipeline's capability to implement line analyses over various wavelengths regimes.

This paper is organized as follows. We briefly describe our observations and data reduction process in Section 2. The classification and physical parameters of LHS 174 from previous studies are reported in Section 3. The spectral synthesis process, selection of atomic and molecular line lists, and abundance formulations are presented in Section 4. The normalization and line selection procedures are detailed in Section 5. Section 6 outlines our methods used to measure elemental abundances and uncertainties for O, Ca, Ti, V, and Fe. Finally, we discuss our resulting abundances and compare them with the values from other studies in Section 7, and summarize the present study in Section 8.

2. Observations

The optical spectrum of the target was observed using the ARC Echelle spectrograph (ARCES) of the Apache Point Observatory (APO) 3.5 m telescope on 2017 September 4 (PIs: Neda Hejazi and Sebastien Lepine). ARCES is a high-resolution, cross-dispersed spectrograph that provides optical spectra with wavelength coverage from 3200 to 10000 Å at a resolving power of $R \sim 33,000$ (9 km s^{-1}) with the $1.6''$ slit. The efficiency of the entire telescope together with the spectrograph system is more than 2.2% at 647 nm, and the spectrograph has an efficiency between 2% and 8% at 630 nm.

For the target, six science frames, each with an exposure time of 600 s and an average air mass of 1.03, were taken. For calibration, ten bias frames, three arc images (using a ThAr lamp), five blue, and ten red flat-field images were taken.⁵ We follow the steps described in the ARCES manual, provided by Karen Kinemuchi,⁶ to reduce our data using standard IRAF routines. We perform cosmic-ray removal, bias subtraction, bad-pixel mask correction, extraction and normalization of the master flat-field spectrum, and extraction of the arc calibration spectra. We then extract the one-dimensional (1D) target spectra and divide them by the normalized master flat field. Finally, we assign the corresponding arcs to the flat-fielded target spectra, which are then wavelength calibrated through the dispersion correction procedure.

We perform a polynomial fit to the spectrum of each echelle order, which approximately represents an empirically determined blaze function for that order. To remove the blaze, we divide the spectrum by the fit, which increases the accuracy of the subsequent continuum/pseudo-continuum normalization (Section 5) required for analysis. The target spectrum has an average SNR of 60, allowing for abundance measurements of some key elements.

3. Classification and Physical Parameters of LHS 174

The metal-poor LHS 174 (PM J03307+3401) is a nearby, high-proper-motion star which is bright enough for high-resolution spectroscopic analyses. The astrometric, photometric, classification, and physical parameters of this star are listed in Table 1. J. E. Gizis (1997) classified LHS 174 by combining metallicity class and spectral type as sdM0.5. A. Y. Kesseli et al. (2019) later reported a combined classification of sdM0.0 for this star. More recently, N. Hejazi et al. (2020) classified the target as esdM1.0 using a template-

⁵ We took twice as many red flat-field as blue flat-field frames because M dwarfs have more flux in longer wavelengths than shorter ones.

⁶ http://astronomy.nmsu.edu/apo-wiki/lib/exe/fetch.php?media=wiki:arcres:kinemuchi_arcres_cookbook.pdf

Table 1
The Astrometry, Photometry, Classification, and Physical Parameters of LHS 174

Property's Name	Description	Value	Reference
Astrometry			
R.A.	Right ascension	03 30 44.82	Gaia Collaboration et al. (2023)
decl.	decl.	+34 01 07.19	Gaia Collaboration et al. (2023)
PM _{RA} (mas yr ⁻¹)	Proper motion in R.A.	497.882	Gaia Collaboration et al. (2023)
PM _{DEC} (mas yr ⁻¹)	Proper motion in decl.	-1499.311	Gaia Collaboration et al. (2023)
π (mas)	Parallax	36.654	Gaia Collaboration et al. (2023)
D (pc)	Distance	27.28	Gaia Collaboration et al. (2023)
RV (km s ⁻¹)	Radial velocity	-230.43	Gaia Collaboration et al. (2023)
Photometry			
G	Gaia G magnitude	12.035	Gaia Collaboration et al. (2023)
G_{BP}	Gaia BP magnitude	12.980	Gaia Collaboration et al. (2023)
G_{RP}	Gaia RP magnitude	11.070	Gaia Collaboration et al. (2023)
J	2MASS J magnitude	9.844	R. M. Cutri et al. (2003)
H	2MASS H magnitude	9.350	R. M. Cutri et al. (2003)
K	2MASS K magnitude	9.143	R. M. Cutri et al. (2003)
Classification			
MC+SpType	Metallicity class+Spectral type	sdM0.5	J. E. Gizis (1997)
MC+SpType	Metallicity class+Spectral type	sdM0.0	A. Y. Kesseli et al. (2019)
MC+SpType	Metallicity class+Spectral type	esdM1.0	N. Hejazi et al. (2020)
SubMC	Metallicity subclass	7 (esdM _r)	N. Hejazi et al. (2020)
Physical Parameters			
T_{eff} (K)	Effective temperature	3790 ± 65 ^a	V. M. Woolf & G. Wallerstein (2005)
T_{eff} (K)	Effective temperature	3800 ± 100	A. Y. Kesseli et al. (2019)
[M/H]	Overall metallicity	-0.95 ± 0.14 ^a	V. M. Woolf & G. Wallerstein (2005)
[M/H]	Overall metallicity	-0.63 ± 0.30	A. Y. Kesseli et al. (2019)
log(g)	Surface gravity	4.78 ± 0.12 ^a	V. M. Woolf & G. Wallerstein (2005)
ξ (km s ⁻¹)	Microturbulent velocity	1.00 ± 0.10 ^a	V. M. Woolf & G. Wallerstein (2005)

Note.

^a There is no reported uncertainty for [M/H] and ξ in V. M. Woolf & G. Wallerstein (2005) and an error value for each of these two parameters has been assigned. The original uncertainties of T_{eff} and log(g) presented by V. M. Woolf & G. Wallerstein (2005) have been modified (Section 3).

fit method through a set of empirically assembled M dwarf classification templates based on the measurements of the TiO and CaH molecular bands. J. Zhong et al. (2015) presented a finer metallicity classification scale by splitting each class of dM (metal-rich M dwarf), sdM, esdM, and usdM into three subclasses, labeled by “r” for the metal-rich, “s” for the standard, and “p” for the metal-poor subclasses (e.g., sdM_r, sdM_s, sdM_p), resulting in 12 metal subclasses in total. N. Hejazi et al. (2020) also employed this classification scheme, though simply numbered the 12 subclasses from 1 for the most metal-rich M dwarfs (dMr) to 12 for the most metal-poor ultra M subdwarfs (usdMp), and assigned a metal subclass of 7 (esdM_r) to LHS 174.

The Galactic velocity components relative to the Galactic center, i.e., U (positive when pointing toward the Galactic center), V (positive when pointing in the direction of the Galactic disk orbital motion), and W (positive when pointing toward the north Galactic pole), of LHS 174, $[U, V, W] = [-177.42, -21.15, -32.47]$ km s⁻¹, indicate its association with the halo.⁷ The disk stars generally tend to move in nearly circular orbits around the Galactic center with

V components around +220 km s⁻¹ and relatively low absolute values of U and W components, as opposed to the random motion of halo stars that move around the Galactic center in different directions (see N. Hejazi et al. 2022 and references therein). The star’s relatively high absolute value for the U component and negative value for the V component (i.e., in the opposite direction of the disk orbital motion), along with its low metallicity as compared to typical higher-metallicity disk stars, rule out its disk membership.

WW05 inferred the physical parameters of LHS 174 using its high-resolution optical APO/ARCES spectrum. Since WW05 measured the abundances of only two elements, Ti and Fe, our main goal of reobserving the star was to obtain the spectrum with higher SNR and analyze more elements. Unfortunately, the poor weather conditions (with a substantial cloud coverage) during a significant part of our observation did not allow us to fully achieve this goal. Nevertheless, we have been able to measure two more elements, Ca and V, using their corresponding atomic lines. WW05 derived the T_{eff} , log(g), and [M/H] of the star using an iterative process along with abundances of Fe and Ti (obtained by measuring their equivalent widths). The microturbulence (ξ) parameter was determined by requiring that there should be no slope in Ti abundance as a function of equivalent width (EQW). We generate synthetic spectra associated with the determined parameters by WW05 as shown in Table 1 (Section 4). We find that the synthetic model exhibits an overall good consistency with the observed flux over many spectral lines,

⁷ The Galactic velocity components of our target were calculated using its astrometry, i.e., coordinates (R.A. and decl.), proper motions in R.A. and decl. (PM_{RA} and PM_{DEC}), distance (D) or parallax (π), and radial velocity (RV), as listed in Table 1. We employed the relevant python code as part of `astrolibpy` (<https://github.com/segasai/astrolibpy>), where the components can be corrected for the solar motion relative to the local standard of rest (LSR). An additional correction was then made for the motion of the LSR relative to the Galactic center $[U, V, W] = [0, +220, 0]$ km s⁻¹.

which indicates that these parameter values reliably present the atmospheric properties of the star.

However, there is no uncertainty associated with the $[M/H]$ and ξ values from [WW05](#). We calculate the metallicity of LHS 174 by applying the photometric M dwarf metallicity relation from [C. Duque-Arribas et al. \(2023\)](#) using the absolute G magnitude and color $G_{BP} - G_{RP}$, $[M/H]_{\text{Phot}} = -1.09$ dex, which is different from the metallicity reported in [WW05](#), i.e., $[M/H]_{\text{WW05}} = -0.95$ dex, by 0.14 dex. We therefore assume an uncertainty of 0.14 dex for the star’s metallicity, which is larger than the abundance errors in [WW05](#). We also assume an uncertainty of 0.10 km s^{-1} for the microturbulence parameter. The assumed uncertainties of $[M/H]$ and ξ are nearly the same or even larger than the typical errors from previous high-resolution analyses of M dwarfs ([S. Lindgren et al. 2016](#); [S. Lindgren & U. Heiter 2017](#); [D. Souto et al. 2017, 2020](#); [E. Marfil et al. 2021](#); [N. Hejazi et al. 2023, 2024](#)).

We further modify the uncertainties of T_{eff} and $\log(g)$ reported in [WW05](#) by deriving these parameters again from the current empirical photometric relations. We compute the effective temperature of the star by employing the photometric relation from [A. W. Mann et al. \(2015\)](#) using the colors $G_{BP} - G_{RP}$ and $J - H$, $(T_{\text{eff}})_{\text{Phot}} = 3855 \text{ K}$, which is different from the value presented in [WW05](#), i.e., $(T_{\text{eff}})_{\text{WW05}} = 3790 \text{ K}$, by 65 K. The T_{eff} error (20 K) derived by [WW05](#) is thus too small, and we increase this error to 65 K. On the other hand, the uncertainty of surface gravity from [WW05](#) (0.31 dex) is unusually large compared to the average error of $\log(g)$ from other M dwarf studies as cited above. This is mainly due to the significantly large uncertainty of the parallax ($\pi = 22.6 \pm 7.4 \text{ mas}$, as was available at the time of [WW05](#)’s study) that, along with the K magnitude and bolometric correction BC_K , was used to calculate the bolometric magnitude (M_{bol}). The resulting M_{bol} , together with the star’s mass and T_{eff} , was then employed to derive the star’s surface gravity. We derive the radius and mass of the star by utilizing the photometric relations from [A. W. Mann et al. \(2015\)](#) and [A. W. Mann et al. \(2019\)](#), respectively, using the absolute K magnitude (M_K) obtained by the K magnitude and the highly accurate Gaia Collaboration parallax ($\pi = 36.654 \pm 0.034 \text{ mas}$; [Gaia Collaboration et al. 2023](#)). The inferred radius and mass are used to determine the surface gravity, $\log(g)_{\text{Phot}} = 4.90$, which is different from the value determined by [WW05](#), i.e., $\log(g) = 4.78$, by 0.12 dex, and quite similar to typical uncertainties reported in the above-mentioned M dwarf studies. We thus assume an error of 0.12 dex for surface gravity to be used in this work. All adopted parameter uncertainties are listed in [Table 1](#).

We apply the rule for α enhancement, $[\alpha/\text{Fe}]$, described in [B. Gustafsson et al. \(2008\)](#), where α elements have been scaled as follows: $[\alpha/\text{Fe}] = +0.4$ for $-5.0 \leq [M/H] \leq -1.0$, $[\alpha/\text{Fe}] = -0.4 \times [M/H]$ for $-1.0 \leq [M/H] \leq 0.0$, and $[\alpha/\text{Fe}] = 0.0$ for $[M/H] \geq 0.0$. For $[M/H] = -0.95$, the α enhancement is $[\alpha/\text{Fe}] = +0.38$, which is used as an input for the abundance measurements. We adjust $[\alpha/\text{Fe}]$ when $[M/H]$ is deviated by its error for measuring the systematic errors of abundances ([Section 6.2](#)).

4. Spectral Synthesis, Abundance Formulation, and Line Data

For our abundance analysis, we synthesize model spectra using [Turbospectrum](#) ([R. Alvarez & B. Plez 1998](#); [B. Plez 2012](#)), a

1D, local thermodynamic equilibrium (LTE) radiative transfer code, together with 1D, hydrostatic, and plane-parallel MARCS model atmospheres ([B. Gustafsson et al. 2008](#)) and a selected set of atomic and molecular line lists. We employ the solar abundances reported in [M. Asplund et al. \(2021\)](#), which are updated abundances with respect to the values from [N. Grevesse et al. \(2007\)](#) used in our previous studies ([N. Hejazi et al. 2023, 2024, 2025](#), hereafter [H23](#), [H24](#), and [H25](#), respectively). In this analysis, we use “continuum-normalized” synthetic spectra (hereafter synthetic or model spectra, for simplicity) computed by [Turbospectrum](#), where line depths are measured from unity.

We utilize the interpolation routine developed by [Thomas Masseron](#) to interpolate the MARCS model associated with the star’s physical parameters from [WW05](#) listed in [Table 1](#).⁸ Synthetic spectra are generated using the interpolated model, while abundances are customized by varying the “relative abundance” $\text{ABUND}(X)$ for element X , which can be converted to the “absolute abundance” $A(X)$ by

$$\begin{aligned} A(X) &= \log(N_X/N_H) + 12 \\ &= \text{ABUND}(X) + A(X)_{\odot} + [M/H], \end{aligned} \quad (1)$$

where N_X indicates the number density of element X , N_H indicates the number density of hydrogen, $A(X)_{\odot}$ is the solar absolute abundance of element X , and $[M/H]$ is the star’s overall metallicity. Similarly, if X is an α element:

$$A(X) = \text{ABUND}(X) + A(X)_{\odot} + [M/H] + [\alpha/\text{Fe}], \quad (2)$$

where $[\alpha/\text{Fe}]$ is the star’s α -element enhancement.⁹ The “abundance” $[X/H]$ is computed relative to the solar value using the equation

$$\begin{aligned} [X/H] &= \log(N_X/N_H) - \log(N_X/N_H)_{\odot} \\ &= A(X) - A(X)_{\odot} \\ &= \text{ABUND}(X) + [M/H], \end{aligned} \quad (3)$$

or

$$[X/H] = \text{ABUND}(X) + [M/H] + [\alpha/\text{Fe}] \quad (4)$$

if X is an α element.

We employ the atomic line list from the Vienna Atomic Line Database ([VALD3](#); [T. Ryabchikova et al. 2015](#)),¹⁰ where hyper-fine structure (HFS) data have recently been added ([Y. Pakhomov et al. 2017](#); [Y. V. Pakhomov et al. 2019](#)). We have found slight differences between the atomic line data from [VALD3](#) and [Linemake](#) ([V. M. Placco et al. 2021](#)) for some of our analyzed spectral lines, and we have accordingly replaced the potential energy of the lower level and $\log(gf)$, where g is the statistical weight of the lower level and f is the oscillator strength of the transition, reported in [VALD3](#) by those values reported in [Linemake](#) ([Table 2](#)).¹¹

We also use the most recent molecular TiO line list (the [ExoMol TOTO](#)) from [L. K. McKemmish et al. \(2019\)](#), where a new line database for the main isotopologs of TiO, i.e.,

⁸ <https://marcs.astro.uu.se/software.php>

⁹ In our previous studies ([H23](#), [H24](#), and [H25](#)), the α enhancement $[\alpha/\text{Fe}]$ of the planet-host cool dwarfs with solar or supersolar metallicity was assumed to be zero, and was removed in [Equation \(4\)](#).

¹⁰ <https://vald.astro.uu.se/>

¹¹ The atomic data sets presented in [Linemake](#) primarily originate from the publications of the atomic physics group in the University of Wisconsin (e.g., [J. E. Lawler et al. 2009, 2013](#), among others), and have been updated over time.

Table 2
The Selected Lines Used to Measure the Abundances of LHS 174

Species	Central Wavelength (Å)	$\log(gf)$	χ^2 Window (Å)	Comments
O (using TiO)	7080.220	$[-5.238, 0.440]^a$	7079.98–7080.42	The combination of 475 TiO lines ^a
O (using TiO)	7081.440	$[-5.002, 0.550]^a$	7081.24–7081.65	The combination of 435 TiO lines ^a
Ca I ^b	6102.723	−0.820	6102.15–6103.25	Blended with a weak Ca I line: 6102.439
Ca I ^b	6122.217	−0.340	6121.50–6123.00	
Ca I	6439.075	+0.390	6438.35–6439.93	
Ca I	6455.598	−1.340	6455.27–6455.88	
Ca I	6462.567	+0.262	6462.11–6463.03	Blended with a weak Fe I line: 6462.725
Ca I	6471.662	−0.686	6471.40–6471.95	
Ca I	6493.781	−0.109	6493.40–6494.15	
Ca I	6499.650	−0.818	6499.35–6499.90	
Ca I ^b	6572.779	−4.320	6572.40–6573.15	Blended with a weak Cr I line: 6572.885
Ca II ^b	8498.020	−1.360	8497.35–8498.70	
				Blended with four weak Ca II lines: 8498.077, 8498.098, 8498.129, 8498.233
Ti I	6554.223	−1.150	6554.05–6554.45	
Ti I	6556.062	−1.060	6555.85–6556.30	
Ti I	8377.861	−1.590	8377.58–8378.25	
Ti I ^b	8396.897	−1.780	8396.60–8397.25	
Ti I ^b	8412.357	−1.480	8412.00–8412.75	
Ti I ^b	8426.507	−1.250	8426.15–8426.85	
Ti I	8682.983	−1.790	8682.73–8683.25	
V I ^c			6089.94–6090.45	The combination of 18 HFS V I lines
	6090.19386	−0.700		
	6090.20104	−0.841		
	6090.20736	−1.005		
	6090.20766	−1.540		
	6090.21283	−1.203		
	6090.21292	−1.344		
	6090.21729	−1.290		
	6090.21743	−1.458		
	6090.21953	−2.654		
	6090.22079	−1.312		
	6090.22117	−1.846		
	6090.22285	−2.244		
	6090.22342	−1.403		
	6090.22516	−1.591		
	6090.22526	−2.022		
	6090.22678	−1.897		
	6090.22717	−1.876		
	6090.22742	−1.846		
V I ^c			6111.33–6111.97	The combination of four HFS V lines
	6111.59249	−1.701		
	6111.63213	−1.224		
	6111.65616	−1.224		
	6111.69580	−1.370		
Fe I	5371.489	−1.645	5371.15–5371.80	
Fe I ^b	5434.523	−2.130	5434.03–5434.87	
Fe I ^b	6430.845	−1.950	6430.60–6431.20	
Fe I ^b	8047.617	−4.660	8047.42–8047.85	
Fe I ^b	8387.771	−1.510	8387.25–8388.25	
Fe I ^b	8688.623	−1.200	8688.10–8689.15	
Fe I	8824.220	−1.540	8823.75–8824.65	

Notes.

^a These ranges and line numbers are associated with the region within the χ^2 window, and only the molecular lines of the most abundant isotopolog, ⁴⁸TiO, are counted, though all the five main TiO isotopolog are used to generate our model spectra.

^b The line data originate from Linemake.

^c Our source VLAD atomic line list used in this study shows the wavelengths in three decimal digits. However, for better presentation, we show the HFS lines of vanadium in five decimal digits to distinguish the lines that are very close to each other.

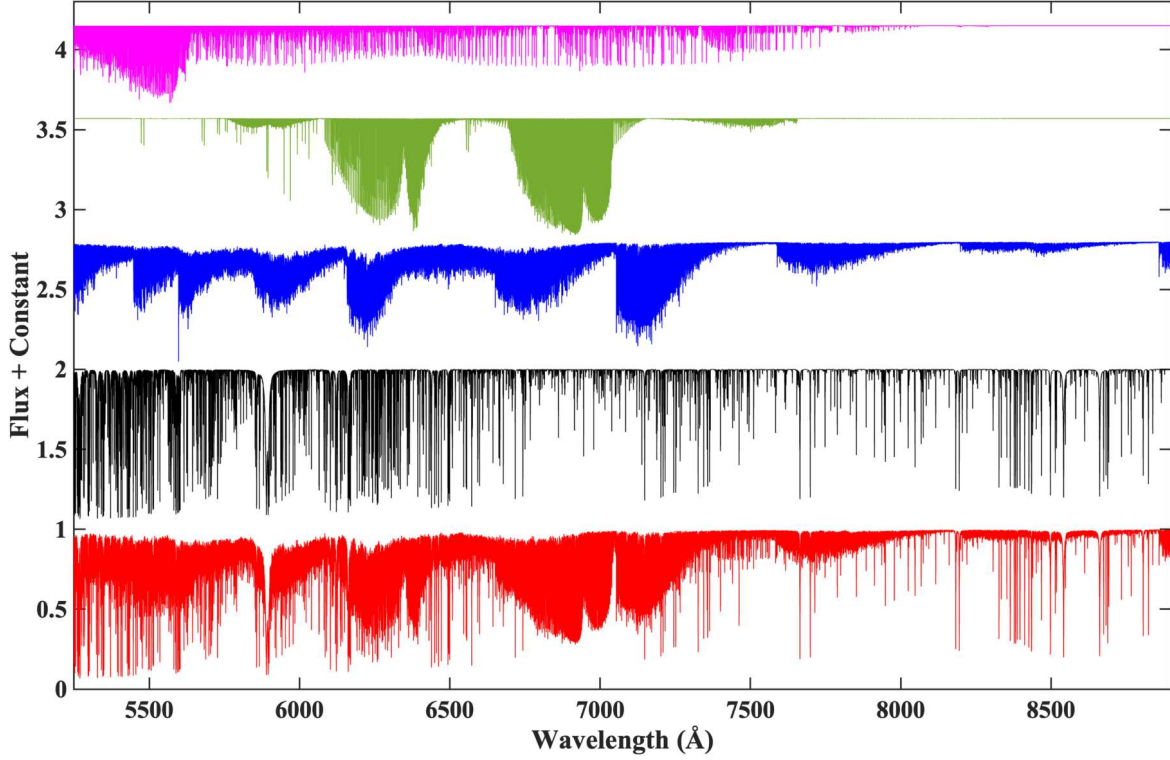


Figure 1. Synthetic models associated with the star’s parameters and default abundances calculated from Equations (1) or (3) assuming $ABUND(X) = 0$ for all elements X when including only MgH molecular lines (magenta), only CaH molecular lines (green), only TiO molecular lines (blue), only atomic lines (black), and all atomic and molecular lines (red).

$^{46}\text{Ti}^{16}\text{O}$, $^{47}\text{Ti}^{16}\text{O}$, $^{48}\text{Ti}^{16}\text{O}$, $^{49}\text{Ti}^{16}\text{O}$, and $^{50}\text{Ti}^{16}\text{O}$, has been presented. The ExoMol TOTO line list includes all dipole-allowed transitions between 13 low-lying electronic states ($X^3\Delta$, $a^1\Delta$, $d^1\Sigma^+$, $E^3\Pi$, $A^3\Phi$, $B^3\Pi$, $C^3\Delta$, $b^1\Pi$, $c^1\Phi$, $f^1\Delta$, and $e^1\Sigma^+$). The rovibronic line positions were obtained by employing potential-energy curves (as simple Morse oscillators),¹² with constant diagonal and off-diagonal spin-orbit and other coupling terms fitted to known empirical energy levels, or to computed ab initio curves if the experimental data were unavailable. The ExoMol TOTO line lists are suitable for effective temperatures below 5000 K, including nearly 60 million transitions for the major TiO isotopologs. However, due to the dissociation of TiO molecules in stellar atmospheres with $T_{\text{eff}} > 4200$ K, TiO line data are not needed to analyze these stars.

Y. V. Pavlenko et al. (2020) have shown that the ExoMol TOTO line list describes the fine details in the line position and intensity of M dwarf spectra more accurately than other TiO line lists. To make our spectral synthesis computationally efficient, we significantly reduce the extremely large number of lines in the ExoMol TOTO line list by choosing stronger lines using the cutoff parameter a (Y. V. Pavlenko et al. 2020):

$$a = (gf) \times \exp(-E_{\text{low}}/kT) > 10^{-6}, \quad (5)$$

where E_{low} is the energy of the lower state, k is the Boltzmann constant, and $T = 3500$ K is the typical effective temperature of M dwarfs. We also include the line lists of other molecular

bands such as VO and CaH (computed by B. Plez 1998), CrH (A. Burrows et al. 2002), MgH (S. Skory et al. 2003 for ^{24}MgH and R. L. Kurucz 2011 for ^{25}MgH and ^{26}MgH), and several more hydrides and oxides. Figure 1 shows the generated synthetic models associated with the star’s fundamental parameters and default abundances inferred from Equations (1) or (3) assuming $ABUND(X) = 0$ for all elements X , when only MgH molecular lines (magenta), only CaH molecular lines (green), only TiO molecular lines (blue), only atomic lines (black), and all atomic and molecular lines (red) are incorporated.

5. Normalization and Line Selection

We perform a careful visual inspection over the entire optical spectrum (3200–10000 Å) of LHS 174. We first remove the spectral ranges that include artifacts, bad pixels, strong noise, and telluric absorption lines due to the Earth’s atmosphere. We then select the spectral lines that are strong enough to be identified from the dominant background molecular lines and are almost isolated from neighboring lines. To reduce the contribution of blending with TiO molecular lines, we exclude those atomic lines that overlap with TiO lines having depths greater than 20% from unity.

The red spectrum in Figure 1 roughly presents the star’s best-fit model (hereafter $\text{Model}_{\text{Approx}}$) and can be used to select the best lines for abundance measurements. We perform a trial-and-error examination for different wavelength intervals within the continuum, or for most cases pseudo-continuum near each side of the lines, which must include at least one or two wavelength data points. These intervals are used in the normalization routine, where the observed spectrum is

¹² A Morse oscillator is a specific kind of bond stretch oscillator commonly used to simulate the anharmonic stretching vibrations of polyatomic molecules in quantum mechanics.

Table 3

The Inferred Abundances and Abundance Sensitivity to Parameter Variation of the Five Analyzed Elements, and Corresponding Systematic, Random, and Total Abundance Errors

Species	Description	O (Using TiO)	Ca	Ti	V	Fe
N	Number of analyzed lines	2	10	7	2	7
[X/H]	Abundance from this work	-0.519 ± 0.081	-0.753 ± 0.177	-0.711 ± 0.144	-1.026 ± 0.077	-1.170 ± 0.135
[X/H]	Abundance from previous studies	-0.37 ± 0.17	...	-0.83 ± 0.07	...	-1.11 ± 0.05
	References	Sch09	...	WW05	...	WW05
$\Delta[X/H]_{T,Neg}$	Abundance change if $\Delta T_{eff} = -65$ K	-0.049	-0.128	-0.101	-0.056	-0.072
$\Delta[X/H]_{T,Pos}$	Abundance change if $\Delta T_{eff} = +65$ K	+0.058	+0.144	+0.114	+0.064	+0.079
$(\Delta[X/H])_T$	Average abundance change	0.054	0.136	0.108	0.060	0.076
$\Delta[X/H]_{M,Neg}$	Abundance change if $\Delta[M/H] = -0.14$ dex	-0.045	-0.056	-0.070	-0.047	-0.087
$\Delta[X/H]_{M,Pos}$	Abundance change if $\Delta[M/H] = +0.14$ dex	+0.050	+0.068	+0.066	+0.047	+0.084
$(\Delta[X/H])_M$	Average abundance change	0.048	0.062	0.068	0.047	0.086
$\Delta[X/H]_{G,Neg}$	Abundance change if $\Delta \log(g) = -0.12$ dex	-0.036	+0.104	+0.056	+0.000	+0.067
$\Delta[X/H]_{G,Pos}$	Abundance change if $\Delta \log(g) = +0.12$ dex	+0.036	-0.078	-0.041	+0.006	-0.052
$(\Delta[X/H])_G$	Average abundance change	0.036	0.091	0.049	0.003	0.060
$\Delta[X/H]_{\xi,Neg}$	Abundance change if $\Delta \xi = -0.10$ km s ⁻¹	-0.011	+0.003	+0.016	+0.008	+0.007
$\Delta[X/H]_{\xi,Pos}$	Abundance change if $\Delta \xi = +0.10$ km s ⁻¹	+0.011	-0.003	-0.018	-0.008	-0.005
$(\Delta[X/H])_{\xi}$	Average abundance change	0.011	0.003	0.017	0.008	0.006
σ_{sys}	Systematic error	0.081	0.175	0.138	0.077	0.130
$\sigma_{ran} = \text{std}/\sqrt{N}$	Random error	...	0.029	0.040	...	0.037
σ_{tot}	Total uncertainty	0.081	0.177	0.144	0.077	0.135

normalized relative to $\text{Model}_{\text{Approx}}$ using a linear fitting (see H24 and H25 for details). The most appropriate continuum/pseudo-continuum “normalizing intervals” are selected when a good agreement between the normalized observed flux and $\text{Model}_{\text{Approx}}$ across these ranges is achieved.

We carry out an additional inspection for the initially selected normalizing intervals around each line and vary the corresponding relative abundance $\text{ABUND}(X)$ by $\Delta \text{ABUND}(X) = \pm 0.300$ dex,¹³ and explore whether the data points in these intervals still show a consistency between the normalized observed data and synthetic model or a considerable discrepancy is evident. On occasions, changing the abundances of specific elements such as oxygen or iron may cause a few weak lines to emerge inside the pseudo-continuum intervals that were apparently line-free regions before the abundance variation. We reselect the normalizing intervals if the abundance variation creates an inconsistency between the normalized observed flux and synthetic model spectrum or/and gives rise to a significant deformation of the pseudo-continuum. It is important to note that in some wavelength areas there are a few (useful) spectral lines that are rather close to each other and can be normalized using the same normalizing intervals, usually on both sides of, and in some cases also inside, those areas. The final selected normalizing intervals are used in normalizing the star’s observed spectrum for the following steps of our analysis.

We manually perform spectral fitting over the lines by varying their corresponding relative abundances from ABUND

$(X) = -0.300$ dex to $\text{ABUND}(X) = +0.300$ dex in steps of 0.100 dex and comparing the normalized observed data with the model spectra. Through visual investigation, we exclude those lines that cannot be fitted with any synthetic model in depth and/or shape. The evident discrepancies can be due to the deficiency in model atmospheres and/or line opacity data sets of low-mass M dwarfs. Other factors such as deviations from LTE may also be a major reason for differences between the observed and model spectra over some spectral lines (T. Olander et al. 2021). High noise levels and strong telluric absorption (and nonstellar) lines distort the star’s spectrum within some wavelength ranges that cannot be matched with model spectra.

When running `AutoSpecFit` (Section 6), we find a few lines that do not result in a well-defined minimum χ^2 value, and we remove these lines from the analysis. Our final selected lines include 28 lines associated with five elements: O (using TiO molecular bands; see Section 7 for details), Ca I (and also one Ca II), Ti I, V I, and Fe I, as shown in Table 2. We search for HFS states of these lines using the VALD3 website through the `Extract Stellar` option, and find that only the two vanadium lines are split into HFS splitting lines.¹⁴ We incorporate these HFS lines in our atomic line list, as shown in the second column of Table 2. The $\log(gf)$ values of the selected lines are listed in the third column of the table. In addition, for each analyzed line we determine a fitting or χ^2 window, where the χ^2 minimization process is performed, as presented in the fourth column of the table.

¹³ This variation range is more than sufficient because the values of $\text{ABUND}(X)$ are typically in the range $[-0.200, +0.200]$ dex in this analysis as well as our previous studies.

¹⁴ The HFS splitting lines are not included in our original atomic line list; instead, the average of all HFS lines as a single line is presented.

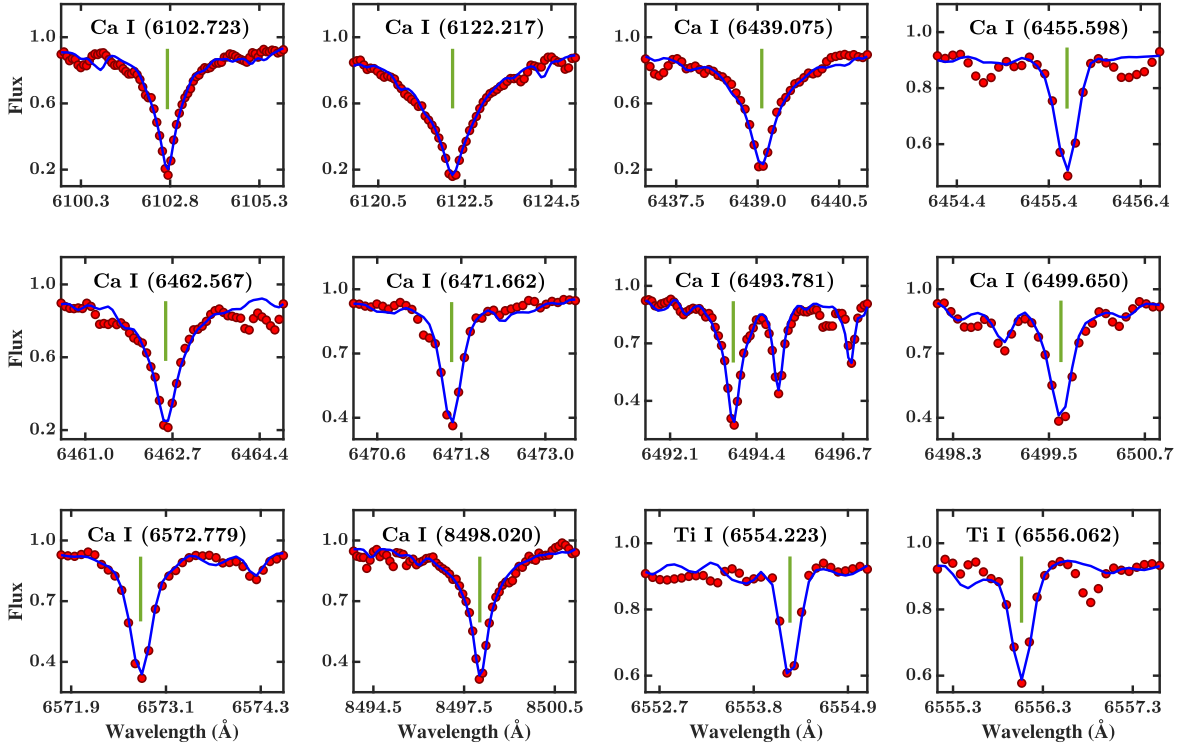


Figure 2. Comparison between the observed spectrum (red dots) and the best-fit model (blue lines) for the analyzed Ca I and Ti I lines of LHS 174. The observed flux is normalized to the best-fit model.

6. Abundance Analysis

6.1. Elemental Abundance Measurements

To measure the elemental abundances of LHS 174, we apply the newly refined version of our automatic spectral fitting code, *AutoSpecFit* (H24), which performs a series of line-by-line χ^2 minimization processes in an iterative manner.¹⁵ The physical parameters (Section 3), the selected normalizing intervals, and the selected χ^2 windows associated with the analyzed lines are employed as input data to run *AutoSpecFit*. The pipeline allows *Turbospectrum* to generate the required synthetic models based on all abundances inferred from each iteration “on the fly”; these synthetic models are then used in the next iteration. Prior to computing χ^2 values, the synthetic spectra are smoothed at the observed spectral resolution using a Gaussian kernel and interpolated at wavelengths that are shifted by the star’s radial velocity. The code then carries out a line-by-line normalization of the observed spectrum with respect to all synthetic models examined in each iteration using the input normalizing intervals. The relative abundance of element X varies from $\text{ABUND}(X) = -0.400$ dex to $\text{ABUND}(X) = +0.400$ dex in steps of 0.020 dex, and a polynomial fit is implemented to the resulting χ^2 values as a function of $\text{ABUND}(X)$ for each relevant line. A relative abundance of $\text{ABUND}(X)_{\text{Line}}$ is assigned to each line, for which χ^2 is minimized. The $\text{ABUND}(X)$ value for element X is the weighted average of $\text{ABUND}(X)_{\text{Line}}$ over all spectral lines corresponding to element X and is optimized through consecutive iterations

until the relative abundances of all analyzed elements converge to their final values simultaneously (see H24 for a comprehensive description of the method). It is important to note that, in general, there is a complex correlation between the abundances of different elements, and simultaneously measuring elemental abundances during an iterative procedure is the best approach to consider this correlation.

Elemental abundances are highly degenerate with physical parameters, and the most reliable method is to keep the parameters fixed when varying abundances. We will further add a routine to a future version of *AutoSpecFit* to modify the parameters between iterations of the abundance inference. In our follow-up study, we investigate the degeneracy between physical parameters and find the spectral regions that are most sensitive to only one parameter. The use of these regions would separate the contribution of different parameters that are simultaneously varied in the spectral fitting and would significantly reduce the parameter degeneracy, leading to more accurate stellar parameters.

Our results are shown in Table 3 for the chemical species (first row), the number of analyzed lines relevant to each species (second row), and the final derived abundances $[X/H]$ (third row). For comparison, the elemental abundances from other studies, if any (fourth row), along with the respective references (fifth row) are also given in this table. We compare the normalized observed spectrum (red dots) and the best-fit synthetic model corresponding to the target’s parameters and derived abundances (blue lines) for the analyzed atomic lines (but assuming $\text{ABUND}(X) = 0$ for all other elements X that are not analyzed in this study) in Figures 2, 3, and 4. Clearly, there is a good agreement between the observed data and best-fit model for the majority of the spectral lines, which indicates the reliability of our technique.

¹⁵ We have recently modified the code slightly for the weighted-average abundance of different lines corresponding to each analyzed element in each iteration of the procedure.

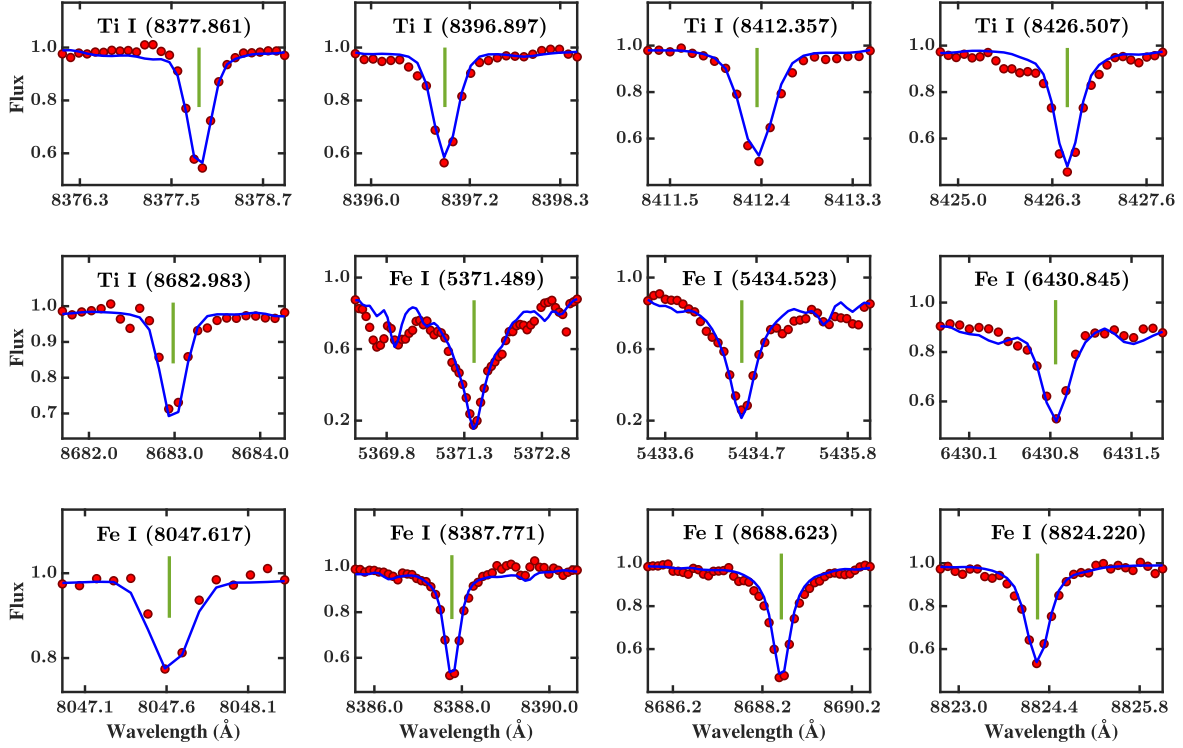


Figure 3. The continuation of Figure 2 for the analyzed Ti I and Fe I lines.

6.2. Abundance Errors

We estimate the uncertainty of the inferred abundances by the quadrature sum of the systematic and random (statistical) errors (Table 3, rows 18 and 19, respectively). The random error is determined using the standard error of the mean, i.e., $\sigma_{\text{ran}} = \text{std}/\sqrt{N}$, where “std” is the standard deviation of the abundances from different lines of each species. However, only two TiO lines (though both lines consist of a large number of TiO lines) and two VI lines (though both lines consist of multiple HFS lines) are analyzed (Table 2), and random error does not apply to these elements. We note that the contribution of random errors is, in general, considerably smaller than that of systematic errors to total uncertainties (last row of Table 3; see also H23, H24, and H25).

The systematic errors are derived by determining the sensitivity of elemental abundances to different physical stellar parameters. To this end, we deviate the four parameters T_{eff} , $[M/H]$, $\log(g)$, and ξ by their associated uncertainties from WW05 (Table 1) in both negative (decreasing, hereafter “Neg”) and positive (increasing, hereafter “Pos”) directions one at a time (Table 3). We then run AutoSpecFit for each case (eight times) with only one parameter deviated in only one direction (Pos or Neg), with the other parameters fixed to the target’s parameters, and then measure the abundances of the analyzed elements. The abundance variations due to the perturbed parameters T_{eff} ($\Delta[X/H]_{T,\text{Neg}}$ and $\Delta[X/H]_{T,\text{Pos}}$), $[M/H]$ ($\Delta[X/H]_{M,\text{Neg}}$ and $\Delta[X/H]_{M,\text{Pos}}$), $\log(g)$ ($\Delta[X/H]_{G,\text{Neg}}$ and $\Delta[X/H]_{G,\text{Pos}}$), and ξ ($\Delta[X/H]_{\xi,\text{Neg}}$ and $\Delta[X/H]_{\xi,\text{Pos}}$) are shown in rows 6–7, 9–10, 12–13, and 15–16 of Table 3, respectively. The average of the absolute values of the two abundance variations due to the deviation of each parameter in

the two Pos and Neg directions is given by

$$\overline{\Delta[X/H]_{\text{P}}} = \frac{|\Delta[X/H]_{\text{P,Neg}}| + |\Delta[X/H]_{\text{P,Pos}}|}{2}, \quad (6)$$

where “P” denotes the parameters, which can be “T” for T_{eff} , “M” for $[M/H]$, “G” for $\log(g)$, and “ ξ ” for ξ , as listed in rows 8, 11, 14, and 17 of Table 3, respectively. The total systematic error σ_{sys} can be calculated by the quadrature sum of the systematic error due to all four parameters P:

$$\sigma_{\text{sys}} = \sqrt{\sum_{\text{P}} [(\overline{\Delta[X/H]_{\text{P}}})^2]}, \quad (7)$$

as shown in row 18 of Table 3. The total abundance uncertainty is determined by the quadrature sum of the random (row 19) and total systematic error:

$$\sigma_{\text{tot}} = \sqrt{\sigma_{\text{ran}}^2 + \sigma_{\text{sys}}^2}, \quad (8)$$

as shown in the last row of Table 3.

7. Discussion

Since metal-poor stars are α enhanced, the abundances of O, Ca, and Ti (i.e., α elements) are markedly higher than the abundances of V and Fe for LHS 174 (Table 3). The abundances of different elements have different sensitivity to the variation of physical parameters. We discuss our results and compare them to previous studies, element by element, in the following sections. In general, differences in abundance measurement techniques, model atmospheres, and line lists used in different studies can give rise to discrepancies in the inferred abundance values of the same element.

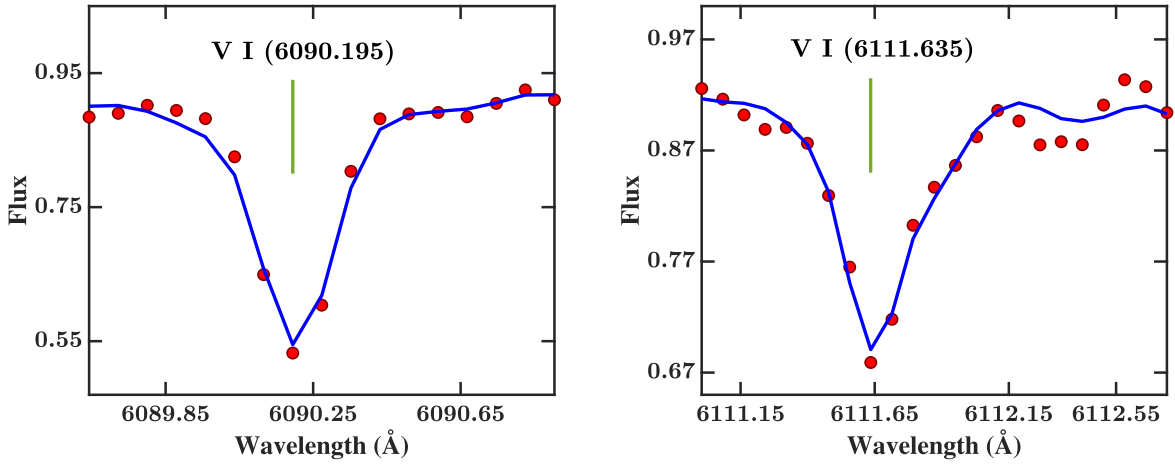


Figure 4. The continuation of Figures 2 and 3 for the analyzed V I lines. The line data used in the spectral synthesis include the HFS splitting lines.

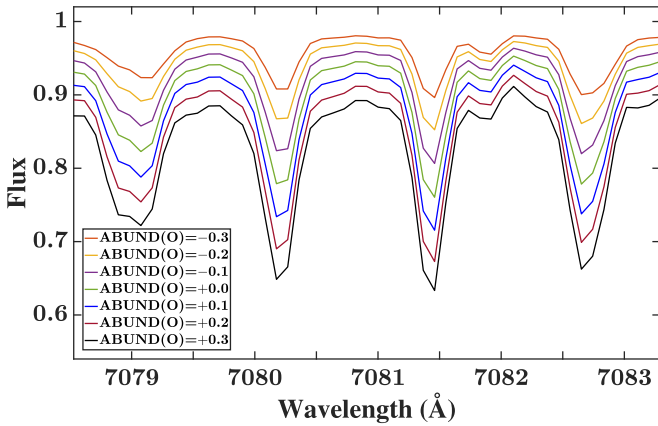


Figure 5. The continuum-normalized synthetic spectra associated with the star's parameters but with different oxygen abundances while assuming $\text{ABUND}(X) = 0$ for other elements X over a small portion of the γ R₂ 0-0 TiO band.

7.1. Oxygen Using TiO Bands

J. A. Valenti et al. (1998) first attempted to perform a detailed examination of TiO lines by modeling the γ R₂ 0-0 TiO band (7078–7103 Å) and fitting to the high-resolution ($R \sim 120,000$) spectrum of the M dwarf GJ 725B (M3.5V) observed using the 2.7 m Harlan J. Smith telescope at McDonald Observatory. J. L. Bean et al. (2006) modified the method of J. A. Valenti et al. (1998) to fit these TiO bands using the high-resolution ($R \sim 50,000$) spectra of five M dwarfs in binary systems with solar-type primaries (using the same telescope used by J. A. Valenti et al. 1998 but with a different instrument setup). Combined with the physical parameters and Fe and Ti abundances determined by WW05, Sch09 measured the abundance of oxygen for 62 late K to early M dwarfs, including LHS 174, using the same TiO fitting technique as J. A. Valenti et al. (1998) and J. L. Bean et al. (2006). Figure 5 shows the sensitivity of a portion of the γ R₂ 0-0 TiO band to the abundance of oxygen, which is similar to the sensitivity of this band to the abundance of titanium, as illustrated in Figure 6. Accurate measurement of the oxygen abundance using TiO bands therefore requires a reliable abundance of titanium, which implies the necessity of

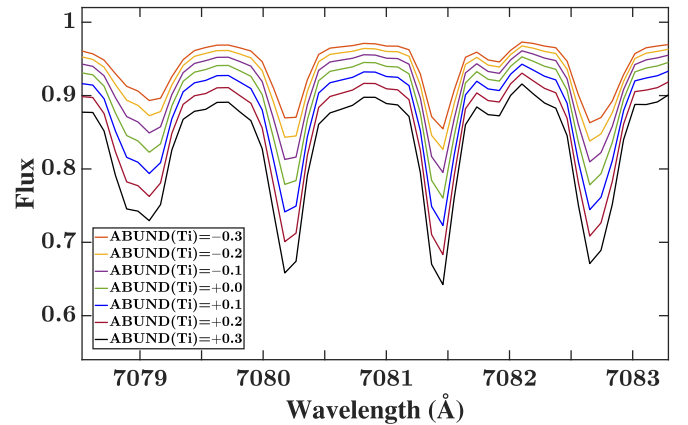


Figure 6. The continuum-normalized synthetic spectra associated with the star's parameters but with different titanium abundances while assuming $\text{ABUND}(X) = 0$ for other elements X over a small portion of the γ R₂ 0-0 TiO band.

simultaneous abundance measurements of different elements during an iterative process.

Sch09 used only a small region of the above-mentioned TiO band from 7077 to 7084.5 Å (excluding the band head) for their oxygen abundance measurements. However, as shown in Figure 1 of Sch09, merely a portion of this region, $\sim 7079.6\text{--}7082.0$ Å, was well modeled for LHS 174 using the updated version of model atmospheres from P. H. Hauschildt et al. (1999) and TiO line list from B. Plez (1998). We also find that this portion is properly modeled using our fitting method, as shown in the top panel of Figure 7, which can be used to infer the oxygen abundance of our target. Each of the two lines consists of a large number of TiO lines with a range of $\log(gf)$ values as shown in Table 2. The bottom panel of Figure 7 compares the normalized observed data with the synthetic model (hereafter Model_{ww05+sch09}) generated using our spectral synthesis method based on the star's physical parameters, Ca and V abundances from this study, but O, Ti, and Fe abundances from other studies, as reported in Table 3. Although the abundances of O, Ti, and Fe from this study are consistent with those from WW05 and Sch09 within their uncertainties, our best-fit model clearly shows a better

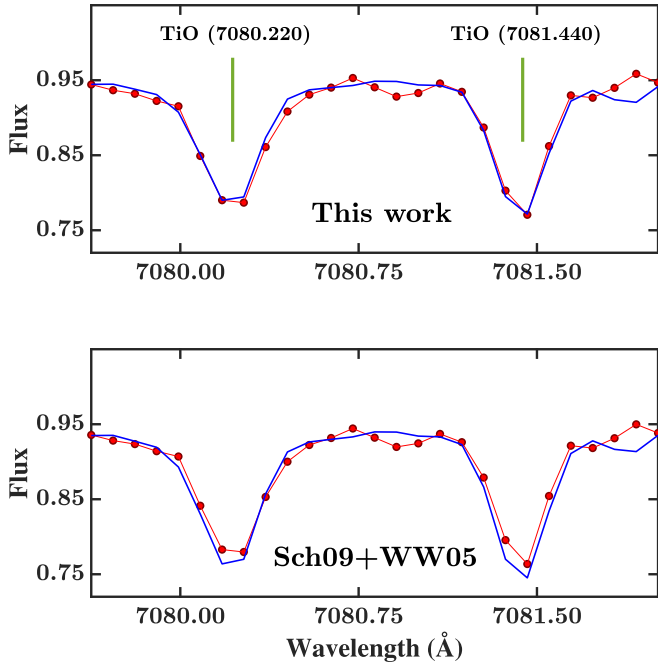


Figure 7. A small portion of the γ R₂ 0-0 TiO band used in measuring the oxygen abundance. Top: comparison between the normalized observed spectrum (red) and the best-fit synthetic model inferred from this study (blue). Bottom: comparison between the normalized observed spectrum (red) and the synthetic spectrum associated with the star’s physical parameters, Ca and V abundances from this study, but O, Ti and Fe abundances from previous studies, as reported in Table 3 (blue, Model_{ww05+Sch09}). The observed spectrum is normalized to each corresponding synthetic model separately.

agreement with the observed spectrum as compared to Model_{ww05+Sch09}.

As can be seen from Table 3, [O/H] is least sensitive to the variation of T_{eff} as compared to the other four elemental abundances. [O/H] has the second least sensitivity to [M/H] (with a minor difference) and $\log(g)$ variations after [V/H]. However, the oxygen abundance shows a moderate sensitivity to ξ . Due to its relatively low sensitivity to the physical parameters, [O/H] has the second least systematic error among the analyzed elements.

7.2. Calcium

Table 3 shows that [Ca/H] is most sensitive to the variation of T_{eff} and $\log(g)$ as compared to the other four elements under study, resulting in the largest systematic error, and in turn the largest total uncertainty. The significantly high sensitivity to T_{eff} and $\log(g)$ motivates us to employ the spectral lines of Ca as diagnostics for determining these two parameters in future M dwarf studies. On the other hand, the calcium abundance is least sensitive to microturbulence ξ , while it has a moderate sensitivity to [M/H] relative to the other elements.

7.3. Titanium

As shown in Table 3, relative to other analyzed elements, the abundance of Ti has a moderate sensitivity to the variation of the two parameters [M/H] and $\log(g)$, but it is most sensitive to ξ . In addition, the titanium abundance has the second highest sensitivity to T_{eff} after [Ca/H]. While the [Ti/H] from this work is consistent with that from WW05 within their uncertainties, our titanium abundance shows a

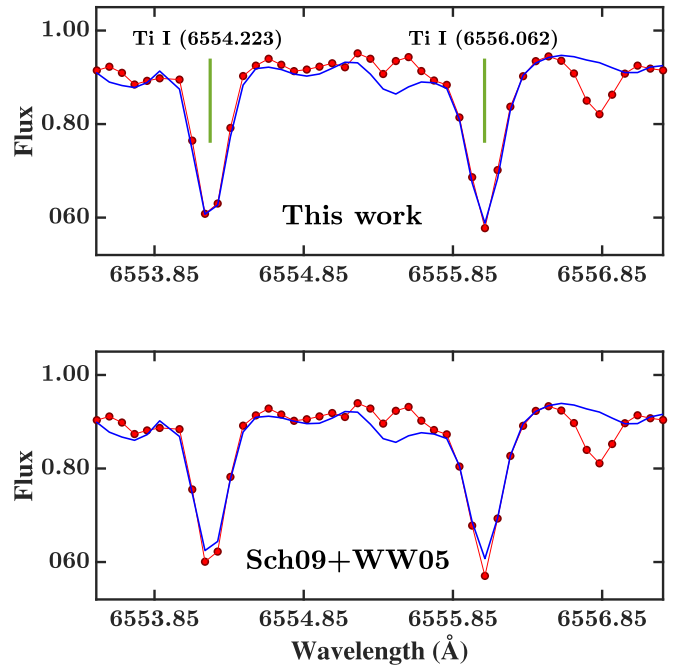


Figure 8. Identical to Figure 7, but for two analyzed Ti I lines.

better agreement with the observed data. Similar to Figure 7, Figure 8 compares the normalized observed spectrum with the best-fit model from this work (top panel) and with Model_{ww05+Sch09} (bottom panel) for two Ti lines. Evidently, our best-fit model is better matched with the observed flux than Model_{ww05+Sch09}.

It is important to note that WW05 measured the abundances of Ti and Fe using EQW analysis. Although EQW analysis is a robust technique to measure stellar elemental abundances, it can give rise to reliable abundances if the EQWs of spectral lines are measured from the continuum level. This method is therefore mainly applicable to hotter FGK dwarfs with a well-defined continuum in their observed spectra. As shown in the top panel of Figure 7, due to the significant contribution of prevailing molecular lines, the fluxes of the (continuum-normalized) best-fit model in the regions around the Ti lines are considerably below unity, and for these lines the continuum level cannot be identified when using the observed spectrum alone. Synthetic spectral fitting as presented in this study is thus a more reliable method to measure the elemental abundances of M dwarfs.

7.4. Vanadium

Y. Shan et al. (2021) characterized a number of V I lines within the 800–910 nm wavelength region using high-resolution (R94600) spectra from the CARMENES survey. They found that many of these lines had a distinctive broad and flat-bottomed shape, resulting from HFS lines, which needed to be incorporated in their atomic line list to infer a reliable vanadium abundance. However, the spectral resolution of our target’s spectrum is significantly lower than that of the CARMENES spectra, and we are unable to detect the flatness around the center of the two V I lines due to the HFS splitting lines. Nevertheless, we include these HFS lines (extracted from the VALD3 website) in our atomic line list to generate more realistic synthetic spectra and determine a more accurate

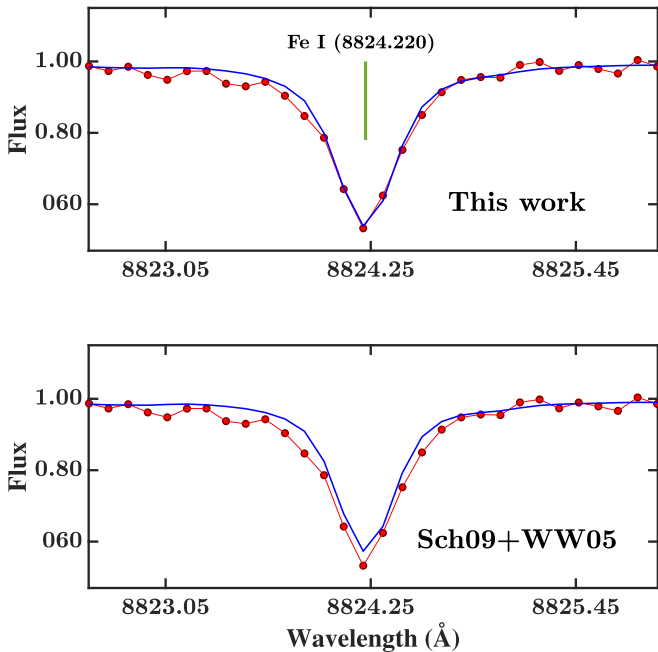


Figure 9. Identical to Figure 7, but for one analyzed Fe I line.

[V/H]. Our results in Table 3 indicate that [V/H] has the least sensitivity to the variation of [M/H] (almost along with [O/H]) and $\log(g)$, and the second least sensitivity to T_{eff} after [O/H]. The vanadium abundance is moderately sensitive to ξ . The rather low sensitivity of [V/H] to the physical parameters has given rise to the smallest systematic error among the other studied elements.

7.5. Iron

As expected, our results in Table 3 show that [Fe/H] has the highest sensitivity to the overall metallicity [M/H] relative to the other four elemental abundances. Historically, [Fe/H] is a proxy of the metallicity since Fe lines are abundant and rather easy to measure in stellar spectra. The iron abundance is moderately sensitive to the deviation of the other three parameters T_{eff} , $\log(g)$, and ξ . Similar to Figures 7 and 8, Figure 9 compares the normalized observed spectrum with the best-fit model from this work (top panel) and with Model_{ww05+sch09} (bottom panel) for a single Fe line. Obviously, the observed data are more consistent with our best-fit model than Model_{ww05+sch09}. Analogous to [Ti/H], WW05 measured [Fe/H] using the EQW method. However, the flux level in spectral regions around some Fe I lines, such as those centered at 5371.489 Å, 5434.523 Å, and 6430.846 Å, are clearly lower than unity (Figure 3), and the EQW analysis is not applicable to determine the abundances of these lines.

8. Summary and Conclusion

We carry out an in-depth spectroscopic analysis of a metal-poor M subdwarf, LHS 174, using its high-resolution optical spectra. We identify 26 atomic lines appropriate for measuring the abundances of four elements, Ca, Ti, V and Fe, as well as a small portion of a TiO band for inferring the abundance of O. As our pilot study, we use a technique, originally developed for NIR spectra, to analyze the star’s optical spectrum, indicating its applicability for measuring the abundances of low-mass stars using different wavelength regimes. Our

automatic pipeline, AutoSpecFit, performs a normalization routine to normalize the observed flux relative to each single synthetic spectrum examined in each χ^2 minimization process, which is of critical importance for a proper comparison between the star’s spectrum and synthetic models. In addition, the code takes into account the complex correlations between the abundances of different elements through an iterative procedure, where the abundances of all analyzed elements inferred from each iteration are incorporated into the synthetic models generated for the next iteration. The process is repeated until globally consistent abundances of all studied elements are achieved simultaneously. Our results exhibit a good agreement between the observed spectrum and the best-fit model constructed based on the target’s parameters and the elemental abundances from this work for the majority of spectral lines. We illustrate that the observed data are better matched with our best-fit model than the synthetic spectra generated using the abundances from previous studies.

The accuracy of our inferred abundances is largely determined by the accuracy of the input physical parameters. Our primary motivation is thus to develop new techniques to reliably determine the physical parameters of M dwarfs. For example, the inferred parameter values can be improved by taking into account the effect of degeneracy between different parameters. Our future follow-up research is an in-depth investigation identifying spectral regions that are essentially sensitive to only one parameter. Utilizing the collected wavelength intervals will isolate the contribution of each parameter to the respective spectral lines and features, and significantly reduce the degeneracy effect between parameters during spectral fitting. The routine of modifying parameters along with abundances will be added to the future version of AutoSpecFit. We emphasize that due to the strong degeneracy between physical parameters and abundances, parameters should be varied and modified between iterations of abundance measurements, not together with abundances.

In addition, the accuracy of our analysis can be improved using spectra with higher SNR, which demands observations with larger telescopes for these low-mass, metal-poor stars. Higher-SNR spectra of metal-poor M subdwarfs would also allow us to measure the abundances of more elements, which could reveal essential information about the nucleosynthesis in the early times of the Galaxy’s formation.

In addition to early-type, metal-poor M subdwarfs, our methodology is applicable to solar and supersolar metallicity as well as cooler (down to 3100 K) M dwarfs, but using high-resolution NIR spectra where H₂O molecular lines dominate (H24, H25, and our ongoing studies). In the NIR regions there are a substantial number of lines that are minimally blended with the prevalent, background H₂O lines, and which can be used for abundance analysis. However, at lower temperatures ($\lesssim 3100$ K) molecular lines become stronger, while the current molecular line lists are still insufficient to properly model many of these undesirable lines that significantly overlap with the lines of important species. This can also hinder efforts to find appropriate normalizing intervals and perform the normalization procedure. Furthermore, MARCS models may not fully consider all physical conditions in the atmosphere of cooler, later-type M dwarfs. For example, dust cloud formation in stars with spectral types of M6 or later may not be adequately treated in MARCS models. The problem with abundance measurements of more metal-rich and/or later-type

M dwarfs may be even more severe in high-resolution optical spectra that include prominent TiO and other molecular lines. Nevertheless, there are still some optical wavelength ranges in early-type, metal-rich M dwarfs where the molecular lines are relatively weak and the spectral lines of some key elements can be identified, provided that the SNR is adequate. A new set of updated PHOENIX model atmospheres by P. Hauschildt et al. (2025, private communication) will be made publicly available in the near future, and is expected to model the atmospheres of cool, late-type M dwarfs more accurately, and can be utilized in follow-up spectroscopic studies.

Acknowledgment

We greatly appreciate the valuable feedback and recommendations from the anonymous reviewer, which enhanced the quality of our manuscript. N.H. acknowledges support from NSF AAG grant No. 2108686 and from NASA ICAR grant No. NNH19ZDA001N. T.N. acknowledges support from the Knut and Alice Wallenberg Foundation. This work used the high-performance computing system of the Physics & Astronomy Department at Georgia State University.

ORCID iDs

Neda Hejazi  <https://orcid.org/0000-0001-5541-6087>
 Sébastien Lépine  <https://orcid.org/0000-0002-2437-2947>
 Thomas Nordlander  <https://orcid.org/0000-0001-5344-8069>
 Wei-Chun Jao  <https://orcid.org/0000-0003-0193-2187>
 David R. Coria  <https://orcid.org/0000-0002-1221-5346>
 Kathryn V. Lester  <https://orcid.org/0000-0002-9903-9911>

References

- Abia, C., Tabernero, H. M., Korotin, S. A., et al. 2020, *A&A*, **642**, A227
 Alvarez, R., & Plez, B. 1998, *A&A*, **330**, 1109
 Asplund, M., Amarsi, A. M., & Grevesse, N. 2021, *A&A*, **653**, A141
 Bean, J. L., Sneden, C., Hauschildt, P. H., Johns-Krull, C. M., & Benedict, G. F. 2006, *ApJ*, **652**, 1604
 Burrows, A., Ram, R. S., Bernath, P., Sharp, C. M., & Milsom, J. A. 2002, *ApJ*, **577**, 986
 Cutri, R. M., Skrutskie, M. F., van Dyk, S., et al. 2003, The IRSA 2MASS All-Sky Point Source Catalog, NASA/IPAC Infrared Science Archive (Washington, DC: NASA)
 Deal, M., Goupil, M. J., Marques, J. P., Reese, D. R., & Lebreton, Y. 2020, *A&A*, **633**, A23
 Dressing, C. D., & Charbonneau, D. 2013, *ApJ*, **767**, 95
 Dressing, C. D., & Charbonneau, D. 2015, *ApJ*, **807**, 45
 Duque-Arribas, C., Montes, D., Tabernero, H. M., et al. 2023, *ApJ*, **944**, 106
 Gaia Collaboration, Vallenari, A., Brown, A. G. A., et al. 2023, *A&A*, **674**, A1
 Gao, X. S., Lind, K., Amarsi, A. M., et al. 2018, *MNRAS*, **481**, 2666
 Gizis, J. E. 1997, *AJ*, **113**, 806
 Grevesse, N., Asplund, M., & Sauval, A. J. 2007, *SSRv*, **130**, 105
 Gustafsson, B., Edvardsson, B., Eriksson, K., et al. 2008, *A&A*, **486**, 951
 Hauschildt, P. H., Allard, F., Baron, E., et al. 1999, *ApJ*, **512**, 377
 Haywood, M. 2008, *MNRAS*, **388**, 1175
 Hejazi, N., Crossfield, I. J. M., Nordlander, T., et al. 2023, *ApJ*, **949**, 79
 Hejazi, N., Crossfield, I. J. M., Souto, D., et al. 2024, *ApJ*, **973**, 31
 Hejazi, N., Lépine, S., Homeier, D., Rich, R. M., & Shara, M. M. 2020, *AJ*, **159**, 30
 Hejazi, N., Lépine, S., & Nordlander, T. 2022, *ApJ*, **927**, 122
 Hejazi, N., Xuan, J. W., Coria, D. R., et al. 2025, *ApJ*, **978**, 42
 Henry, T. J., & Jao, W.-C. 2024, *ARA&A*, **62**, 593
 Kesseli, A. Y., Kirkpatrick, J. D., Fajardo-Acosta, S. B., et al. 2019, *AJ*, **157**, 63
 Kurucz, R. L. 2011, *CajPh*, **89**, 417
 Lawler, J. E., Guzman, A., Wood, M. P., Sneden, C., & Cowan, J. J. 2013, *ApJS*, **205**, 11
 Lawler, J. E., Sneden, C., Cowan, J. J., Ivans, I. I., & Den Hartog, E. A. 2009, *ApJS*, **182**, 51
 Lindgren, S., & Heiter, U. 2017, *A&A*, **604**, A97
 Lindgren, S., Heiter, U., & Seifahrt, A. 2016, *A&A*, **586**, A100
 Lépine, S., Rich, R. M., & Shara, M. M. 2007, *ApJ*, **669**, 1235
 Mann, A. W., Dupuy, T., Kraus, A. L., et al. 2019, *ApJ*, **871**, 63
 Mann, A. W., Feiden, G. A., Gaidos, E., Boyajian, T., & von Braun, K. 2015, *ApJ*, **804**, 64
 Marfil, E., Tabernero, H. M., Montes, D., et al. 2021, *A&A*, **656**, A162
 McKemmish, L. K., Masseron, T., Hoeijmakers, H. J., et al. 2019, *MNRAS*, **488**, 2836
 Michaud, G., Fontaine, G., & Beaudet, G. 1984, *ApJ*, **282**, 206
 Moedas, N., Deal, M., Bossini, D., & Campilho, B. 2022, *A&A*, **666**, A43
 Nordlander, T., Gruyters, P., Richard, O., & Korn, A. J. 2024, *MNRAS*, **527**, 12120
 Olander, T., Heiter, U., & Kochukhov, O. 2021, *A&A*, **649**, A103
 Pakhomov, Y., Piskunov, N., & Ryabchikova, T. 2017, in ASP Conf. Ser. 510, Stars: From Collapse to Collapse, ed. Y. Y. Balega, D. O. Kudryavtsev, I. I. Romanyuk, & I. A. Yakunin (San Francisco, CA: ASP),
 Pakhomov, Y. V., Ryabchikova, T. A., & Piskunov, N. E. 2019, *ARep*, **63**, 1010
 Pavlenko, Y. V., Yurchenko, S. N., McKemmish, L. K., & Tennyson, J. 2020, *A&A*, **642**, A77
 Placco, V. M., Sneden, C., Roederer, I. U., et al. 2021, *RNAAS*, **5**, 92
 Plez, B. 1998, *A&A*, **337**, 495
 Plez, B., 2012 Turbospectrum: Code for Spectral Synthesis, Astrophysics Source Code Library, ascl:1205.004
 Rajpurohit, A. S., Reylé, C., Allard, F., et al. 2014, *A&A*, **564**, A90
 Reid, I. N., & Hawley, S. L. 2000, New Light on Dark Stars. Red Dwarfs, Low-mass Stars, Brown Dwarfs (London: Springer)
 Ryabchikova, T., Piskunov, N., Kurucz, R. L., et al. 2015, *PhyS*, **90**, 054005
 Schmidt, S. J., Wallerstein, G., Woolf, V. M., & Bean, J. L. 2009, *PASP*, **121**, 1083
 Schönrich, R., & Binney, J. 2009, *MNRAS*, **396**, 203
 Shan, Y., Reiners, A., Fabbian, D., et al. 2021, *A&A*, **654**, A118
 Skory, S., Weck, P. F., Stancil, P. C., & Kirby, K. 2003, *ApJS*, **148**, 599
 Souto, D., Cunha, K., García-Hernández, D. A., et al. 2017, *ApJ*, **835**, 239
 Souto, D., Cunha, K., Smith, V. V., et al. 2020, *ApJ*, **890**, 133
 Souto, D., Cunha, K., Smith, V. V., et al. 2022, *ApJ*, **927**, 123
 Tabernero, H. M., Shan, Y., Caballero, J. A., et al. 2024, *A&A*, **689**, A223
 Valenti, J. A., Piskunov, N., & Johns-Krull, C. M. 1998, *ApJ*, **498**, 851
 Woolf, V. M., Lépine, S., & Wallerstein, G. 2009, *PASP*, **121**, 117
 Woolf, V. M., & Wallerstein, G. 2005, *MNRAS*, **356**, 963
 Woolf, V. M., & Wallerstein, G. 2006, *PASP*, **118**, 218
 Woolf, V. M., & Wallerstein, G. 2020, *MNRAS*, **494**, 2718
 Zhong, J., Lépine, S., Hou, J., et al. 2015, *AJ*, **150**, 42